

# High-Efficiency Class- $iF^{-1}$ Power Amplifier With Enhanced Linearity

Chenhao Chu<sup>1</sup>, Member, IEEE, Vivek Tamrakar<sup>2</sup>, Member, IEEE, Sagar K. Dhar<sup>3</sup>, Member, IEEE, Tushar Sharma<sup>4</sup>, Member, IEEE, Jayanta Mukherjee<sup>5</sup>, Senior Member, IEEE, and Anding Zhu<sup>6</sup>, Fellow, IEEE

**Abstract**—This article presents a new class of power amplifier (PA), designated as Class- $iF^{-1}$ , that utilizes input harmonics to achieve high efficiency with enhanced linearity performance beyond the conventional Class- $F^{-1}$  PA. The amplitude-to-amplitude modulation (AM/AM) profile of the conventional Class- $F^{-1}$  PA is mathematically modeled as a function of the input drive level, such that the occurrence of inflection points can be investigated. Theoretical derivation shows that the appropriate utilization of input nonlinearity poses a solution to rectify the double inflection characteristics of the conventional Class- $F^{-1}$  PA, which, consequently, can be realized by proper manipulation of second harmonic source impedance ( $Z_{2S}$ ). The theoretical findings were validated with load–pull results at 2.3 GHz with a 2-mm gallium nitride (GaN) device, presenting enhanced linearizable output power and efficiency for the Class- $iF^{-1}$  PA, with a broad second harmonic design space over the open-circuit region. As proof of concept, a Class- $iF^{-1}$  PA was designed and fabricated, obtaining 40.1–40.8 dBm output power and 71.2%–77.3% drain efficiency (DE) performance at 3-dB gain compression level operating over 2.0–2.6-GHz frequency range. When tested with a 20-MHz 8.5-dB peak-to-average-power-ratio (PAPR) long-term evolution (LTE) signal, around 32.01-dBm average output power was attained at 2.3 GHz with an average DE of 34.59% and –56.05 dBc adjacent channel power ratios (ACPRs) after digital predistortion (DPD) correction.

**Index Terms**—Amplitude-to-amplitude modulation (AM/AM), Class- $F^{-1}$ , Class- $iF^{-1}$ , gallium nitride (GaN), harmonic tuning, input nonlinearity, power amplifier (PA).

## I. INTRODUCTION

THE demand for highly efficient, wideband, and linear power amplifiers (PAs) has been drawing considerable attention in various industrial applications. To achieve high efficiency with optimal saturated output power, harmonic tuned

PAs are realized by minimizing the overlap between the drain current and voltage waveforms and increasing the drain voltage fundamental amplitude via a proper manipulation of harmonic load impedance [1], [2], [3], [4], [5], [6], [7], [8]. To enable wideband operation, continuous-mode theory has been proposed by sweeping the load harmonic impedance along the open/short-circuit regions, which in turn provides the flexible design space for load fundamental impedance [9], [10], [11], [12], [13], [14], [15], [16], [17].

Recently, input nonlinearity of gallium nitride (GaN) transistors has attracted significant interest since the nonlinear  $C_{GS} - V_{GS}$  profile generates a harmonic voltage at the intrinsic gate node of the active device, which can modify the gate and drain waveforms [18], [19], [20], [21], [22], [23], [24], [25], [26]. Therefore, by properly tuning the second harmonic source impedance, the efficiency of the PA can be improved. Furthermore, new source/load design spaces have been reported for both harmonic tuned and continuous-mode PAs, such as Class-B/J, Class- $F/F^{-1}$ , and continuous Class- $F/F^{-1}$  [18], [19], [20], [21], [22], [23], [24], [25], [26].

Among them, the Class- $F^{-1}$  PA has gained a significant amount of research interest because of its high drain efficiency (DE) performance (theoretically 91%) at saturation [18], [19], [20], [22], [23], [25], [27]. Unfortunately, Class- $F^{-1}$  PA shows severe nonlinearity, exhibiting unique continuous-wave (CW) amplitude-to-amplitude modulation (AM/AM) characteristic with two inflection points [19], [20], [21], [25], [27], [28], as shown in Fig. 1(a), where the first inflection occurs at low power, while the second inflection happens at the saturation power level. Such a nonlinear profile restrains the Class- $F^{-1}$  PA being deployed in some practical applications.

To resolve the highly nonlinear double inflection characteristics in the conventional Class- $F^{-1}$ , a new class of PA, called “Class- $iF^{-1}$ ,” has been proposed in [29], by introducing a concept of terminating the second harmonic source impedance ( $Z_{2S}$ ) with open circuit instead of conventional short circuit, which results in a flat gain profile as shown in Fig. 1(b). Due to the page limit of the conference paper, no detailed analysis was given. In this article, we extend the concept with further theoretical derivations and system analysis. To explain the double inflection characteristic in the AM/AM profile of Class- $F^{-1}$  PA, a comprehensive derivation with a set of new current modeling is given so that the time-domain gate–drain waveforms and the AM/AM profile can be analyzed versus

Manuscript received 30 July 2022; revised 4 November 2022; accepted 6 November 2022. Date of publication 1 December 2022; date of current version 5 May 2023. This work was supported in part by the Science Foundation Ireland under Grant 16/IA/4449 and Grant 17/NSFC/4850. (Corresponding author: Chenhao Chu.)

Chenhao Chu and Anding Zhu are with the School of Electrical and Electronic Engineering, University College Dublin, Dublin 4, D04 V1W8 Ireland (e-mail: chenhao.chu@ucdconnect.ie; anding.zhu@ucd.ie).

Vivek Tamrakar and Jayanta Mukherjee are with the Department of Electrical Engineering, IIT Bombay, Powai, Mumbai, Maharashtra 400076, India (e-mail: vivekee@ee.iitb.ac.in; jayanta@ee.iitb.ac.in).

Sagar K. Dhar and Tushar Sharma are with Renesas Electronics Corporation, San Diego, CA 92014 USA (e-mail: sagar.dhar.vz@renesas.com; sharma.tushar17@ieee.org).

Color versions of one or more figures in this article are available at <https://doi.org/10.1109/TMTT.2022.3224132>.

Digital Object Identifier 10.1109/TMTT.2022.3224132

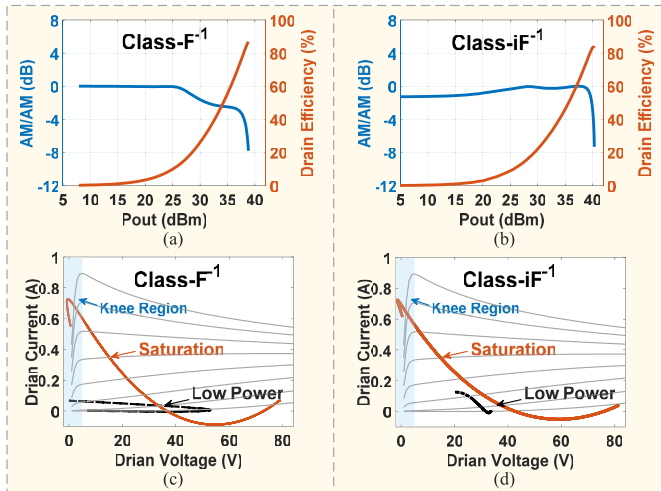


Fig. 1. Comparison between Class-F<sup>-1</sup> and Class-iF<sup>-1</sup> for a 2-mm GaN device at 2.3 GHz. (a) and (b) AM/AM profile. (c) and (d) Loadlines at low power and saturation power levels.

different output power level and input nonlinearity parameters. It is then theoretically derived that, by varying the value of one specific input nonlinearity parameter, the first inflection point can be shifted to a higher output power level. The loadline of the PA can avoid entering the knee region at the low power level, as shown in Fig. 1(c) and (d). This explains the root cause of the double inflection characteristics of a conventional Class-F<sup>-1</sup> PA and identifies the solution to it. To the best of the author's knowledge, this is also the first time that the drain current and voltage waveforms are modeled as a function of power driving level and input nonlinearity. The theoretical analysis and experimental validation confirm that a high-efficiency Class-iF<sup>-1</sup> PA can be designed with the second harmonic source impedance ( $Z_{2S}$ ) over the open-circuit region of  $\angle\Gamma_{2S} = [-90^\circ, 90^\circ]$ .

The remainder of this article is organized as follows. Section II presents the theory of the proposed Class-iF<sup>-1</sup> PA. Section III shows the load—pull PA performance with different input nonlinearity, namely, different second harmonic source manipulation. The design procedure of a Class-iF<sup>-1</sup> PA and the experimental validation are presented in Section IV, with a conclusion in Section V.

## II. THEORETICAL ANALYSIS OF CLASS-iF<sup>-1</sup> PA

The input nonlinearity of an active device is a result of the nonlinear gate to source capacitance ( $C_{GS}$ ) profile, which varies as a function of both the gate–source voltage ( $V_{GS}$ ) and the drain–source voltage ( $V_{DS}$ ) [18], [19], [20], [21], [22], [23], [24], [25], [26]. For the conventional harmonically tuned PAs, an ideal sinusoidal excitation is assumed at the input of the device. However, as shown in Fig. 2(a), the nonlinear  $C_{GS}$ – $V_{GS}$  profile generates out-of-phase second harmonic voltages at the intrinsic gate node of the device and results in the alternation of the input sinusoidal waveform [30], [31], [32], [33].

Although the intrinsic gate and drain waveforms have been derived versus input nonlinearity in the previously reported papers [18], [19], [20], [21], [22], [23], [24], [25], [26], [27],

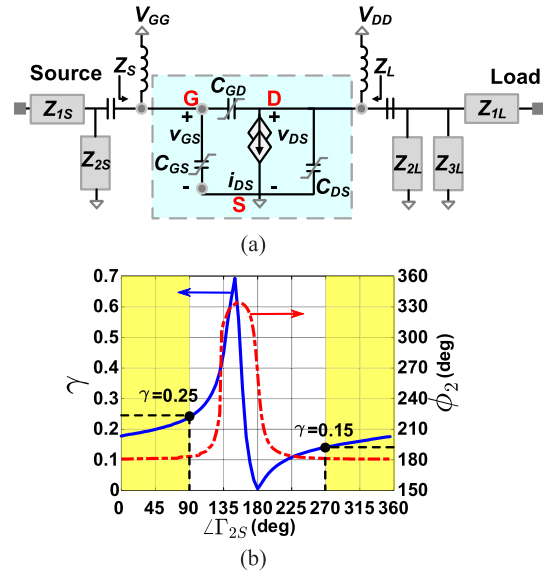


Fig. 2. (a) Simplified nonlinear circuit model for GaN device. (b) Input nonlinearity parameters  $\gamma$  and  $\phi_2$  versus  $\angle\Gamma_{2S}$  with  $|\Gamma_{2S}| = 0.9$ .

[28], the analyses were generally focused on the saturated output power level, which is limited for explaining and predicting the inflection points in AM/AM profile for the conventional Class-F<sup>-1</sup> [19], [20], [21], [25], [27], [28]. To fully understand it, namely, the double inflection characteristics in the AM/AM profile, we revisited the time-domain drain current and voltage waveform with the consideration of input nonlinearity, while maintaining the same load terminations with conventional Class-F<sup>-1</sup>, where second harmonic load ( $Z_{2L}$ ) is open circuit and third harmonic load ( $Z_{3L}$ ) is short circuit. The time-domain waveforms modeling is presented in detail in Sections II-A–II-C.

### A. Gate Waveform Shaping

Assuming the device is excited by a sinusoidal input signal and considering up to second harmonic source impedance, the generalized gate voltage waveform can be expressed as

$$\begin{aligned} v_{GS}(\theta) &= V_{GS0} + V_{GS1} \cos \theta + V_{GS2} \cos (2\theta + \phi_2) \\ &= V_{GS0} + V_{GS1} [\cos \theta + \gamma \cos (2\theta + \phi_2)] \end{aligned} \quad (1)$$

where  $V_{GS0}$  is the dc gate bias voltage, and  $V_{GS1}$  and  $V_{GS2}$  are the fundamental and second harmonic gate voltage components, respectively. Two nonlinearity parameters,  $\phi_2$  and  $\gamma$ , are defined to describe the input nonlinear characteristics, where  $\phi_2$  is the phase difference between  $V_{GS2}$  and  $V_{GS1}$ , and  $\gamma = V_{GS2}/V_{GS1}$  denotes the normalized magnitude of the second harmonic gate voltage with respect to the fundamental voltage. Fig. 2 shows the input nonlinearity parameters  $\gamma$  and  $\phi_2$  for a 2-mm GaN device [25]. With respect to the second harmonic source phase  $\angle\Gamma_{2S}$ , the value of  $\gamma$  varies from 0 to 0.7. While the value of  $\phi_2$  changes over  $(170^\circ, 320^\circ)$ ,  $\phi_2$  keeps that value of  $180^\circ$  in most of cases. For simplicity, the analysis is under the circumstance of  $\phi_2 = 180^\circ$ , with which the  $\gamma$  value varies from 0.15 to 0.25, while  $Z_{2S}$  sweeps over the region  $\angle\Gamma_{2S} = [0^\circ, 90^\circ] \cup [270^\circ, 360^\circ]$  (or  $[-90^\circ, 90^\circ]$ ).

Generally, the class of PA operation can be categorized based on the device conduction angle  $\alpha$ , namely, the bias condition. Herein,  $\alpha$  is the value with the assumption of a second harmonic source short circuit. However, the input nonlinearity changes the conduction angle from the original value of  $\alpha$  [21], [23]. The modified conduction angle,  $\beta$ , for a Class-B bias condition ( $\alpha = \pi$ ) can be found by solving

$$\cos \frac{\beta}{2} + \gamma \cos(\beta + \phi_2) = \cos \frac{\alpha}{2}. \quad (2)$$

### B. Drain Current Waveform Modeling

To quantify the PA performance at different output power levels, herein, we define a new parameter,  $\rho$ , as the input voltage scaling factor. To analyze the double inflection characteristic, a comprehensive derivation is conducted with the drain current waveform with respect to power driving level: the low-power (preinflection) region with  $0 \leq \rho \leq \rho_1$ , and the high-power (post-inflection) region with  $\rho_1 < \rho \leq 1$ . Hence, drain current waveform modeling is derived as

$$i_{\text{DS,iF}^{-1}}(\theta) = \begin{cases} i_{\text{DS,B}}(\theta), & 0 \leq \rho < \rho_1 \\ i_{\text{DS,F}^{-1}}(\theta), & \rho_1 \leq \rho < 1. \end{cases} \quad (3)$$

According to (2), for an active device with constant transconductance ( $g_m$ ), the generalized bias-dependent drain current waveform can be defined as

$$i_{\text{DS}}(\theta) = \begin{cases} \rho \cdot I_{\text{max}} \left[ \frac{\cos \theta - \cos \frac{\alpha}{2}}{1 - \cos \frac{\alpha}{2}} + \gamma (\cos 2\theta + \phi_2) \right], & |\theta| \leq \frac{\beta}{2} \\ 0, & -\alpha \leq \theta \leq -\frac{\beta}{2}, \frac{\beta}{2} \leq \theta \leq \alpha \end{cases} \quad (4)$$

where  $I_{\text{max}}$  is the maximum current limit of the device. Under the previous Class-B biasing, by substituting  $\alpha = \pi$  to (2) and (4), the generalized drain current before the first inflection point, namely  $0 \leq \rho \leq \rho_1$ , can be expressed as

$$i_{\text{DS,B}}(\theta) = \begin{cases} \rho \cdot I_{\text{max}} [\cos \theta + \gamma (\cos 2\theta + \phi_2)], & |\theta| \leq \frac{\beta}{2} \\ 0, & -\pi \leq \theta \leq -\frac{\beta}{2}, \frac{\beta}{2} \leq \theta \leq \pi. \end{cases} \quad (5)$$

To further evaluate the inflection point and find a solution for the conventional Class-F<sup>-1</sup>, the drain current waveform is different from (5) after the power driving level  $\rho_1$ . Load impedance conditions with the second harmonic ( $Z_{2L}$ ) open circuit and third harmonic ( $Z_{3L}$ ) need to be considered for proper drain current modeling. Although the intrinsic current waveform  $i_{\text{DS,F}^{-1}}$  attempts to generate the second harmonic component  $i_2$ , it cannot be achieved due to infinite  $Z_{2L}$ . Hence,

under the input nonlinearity, the drain current waveform within power level,  $\rho_1 < \rho \leq 1$ , can be expressed as

$$i_{\text{DS,F}^{-1}}(\theta) = \begin{cases} \rho \cdot I_{\text{max}} [\cos \theta + \gamma (\cos 2\theta + \phi_2)] - i_2, & |\theta| \leq \frac{\beta}{2} \\ 0, & -\pi \leq \theta \leq -\frac{\beta}{2}, \frac{\beta}{2} \leq \theta \leq \pi \end{cases} \quad (6)$$

where

$$i_2 = \Psi_r \cos 2\theta - \Psi_q \sin 2\theta \quad (7)$$

herein,  $\Psi_r$  and  $\Psi_q$  denote the coefficients for real and reactive terms of second harmonic drain current, respectively.

In both (4) and (6), there is no surprise that the coefficient of reactive term  $\Psi_q$  appears to be a function of  $\gamma$  and  $\phi_2$  due to the input second harmonic nonlinearity. By using the Fourier transformation for (4) and (5), the dc ( $I_{\text{dc}}$ ), fundamental ( $I_1$ ), second harmonic ( $I_2$ ), and third harmonic ( $I_3$ ) components can be calculated as functions of  $\rho$ ,  $\beta$ ,  $\gamma$ , and  $\phi_2$  as (8)–(14), shown at the bottom of the next page, where  $I_{nr}$  and  $I_{nq}$  ( $n = 1, 2, 3$ ) represent the real and reactive current components, respectively. Fig. 3(a)–(c) shows the normalized intrinsic drain current waveforms versus power driving level with  $\gamma = 0, 0.2, 0.35$ , respectively. The waveforms for  $\gamma = 0.35$  have lower ripple, whereas clipping happens at  $\rho = 0.2$  for  $\gamma = 0$ .

### C. Drain Voltage Modeling

To analyze the drain voltage components, the fundamental and harmonic load impedance conditions are needed and can be expressed as

$$\begin{aligned} Z_{1L} &= \frac{\sqrt{2}}{2 \left( \frac{1}{2} - \frac{8}{9\pi^2} \right)} R_{\text{opt}} \\ Z_{2L} &= \infty \\ Z_{3L} &= 0 \end{aligned} \quad (15)$$

where  $R_{\text{opt}}$  is the optimal fundamental load impedance at Class-B operation and is defined as  $R_{\text{opt}} = (V_{\text{DD}} - V_K)/(0.5I_{\text{max}})$ . Herein,  $V_{\text{DD}}$  denotes the drain voltage dc component, and  $V_K$  is the knee voltage.

Hence, the drain voltage can be evaluated by using the impedance values in (15). At the first inflection point  $\rho_1$ , the drain voltage hits the knee voltage region ( $V_K$ ). Assuming knee voltage to be zero ( $V_K = 0$ ), the voltage swing at the intrinsic drain node can be expressed as a function of drain voltage fundamental ( $V_1$ ), second harmonic ( $V_2$ ), and third harmonic ( $V_3$ ) components

$$v_{\text{DS,swing}} = V_1 + V_2 + V_3 \quad (16)$$

where

$$V_1 = I_1 Z_{1L}, \quad V_2 = I_2 Z_{2L}, \quad V_3 = I_3 Z_{3L}. \quad (17)$$

For simplicity, the load terminations are considered only resistive in the following analysis. When the voltage swing

$V_{DS,swing}$  equals to  $V_{DD}$ , the driving level reaches the inflection point  $\rho_1$ . The value of  $Z_{2L}$  can be chosen as ten times the value of fundamental impedance  $Z_{1L}$  or higher based on the practicality of realization for Class-F<sup>-1</sup> mode of operation. On further increasing the driving level  $\rho$ , the drain voltage swing  $V_{DS,swing}$  remains fixed as  $V_{DD}$ . This is due to the fact that the loadline keeps hitting the knee region with the

drain voltage swing of  $V_{DD}$ . The second harmonic current component should be maintained at zero until the saturated output power level with  $\rho = 1$ . As such, the second harmonic current  $i_2$  coefficients  $\Psi_r$  and  $\Psi_q$  can be calculated by solving the expressions given as

$$I_{1r}Z_{1L} + I_{2L}Z_{2L} = V_{DD} - V_K, \quad I_{2q} = 0. \quad (18)$$

$$I_{dc} = \begin{cases} \rho I_{max} \left( \frac{2 \sin \frac{\beta}{2} + \gamma \cos \phi_2 \sin \beta}{2\pi} \right), & 0 \leq \rho < \rho_1 \cap |\theta| \leq \frac{\beta}{2} \\ \rho I_{max} \left( \frac{2 \sin \frac{\beta}{2} + \gamma \cos \phi_2 \sin \beta - \Psi_r \sin \beta}{2\pi} \right), & \rho_1 \leq \rho < 1 \cap |\theta| \leq \frac{\beta}{2} \\ 0, & \text{otherwise} \end{cases} \quad (8)$$

$$I_{1r} = \begin{cases} \rho I_{max} \frac{3\beta + 3 \sin \beta + 2\gamma \cos \phi_2 \left( 3 \sin \frac{\beta}{2} + \sin \frac{3\beta}{2} \right)}{6\pi}, & 0 \leq \rho < \rho_1 \cap |\theta| \leq \frac{\beta}{2} \\ \rho I_{max} \frac{3\beta + 3 \sin \beta + 2\gamma \cos \phi_2 \left( 3 \sin \frac{\beta}{2} + \sin \frac{3\beta}{2} \right)}{6\pi} - \Psi_r \frac{3 \sin \frac{\beta}{2} + \sin \frac{3\beta}{2}}{3\pi}, & \rho_1 \leq \rho < 1 \cap |\theta| \leq \frac{\beta}{2} \\ 0, & \text{otherwise} \end{cases} \quad (9)$$

$$I_{1q} = \begin{cases} -\rho I_{max} \frac{\gamma \sin \phi_2}{3\pi} \left( 3 \sin \frac{\beta}{2} - \sin \frac{3\beta}{2} \right), & 0 \leq \rho < \rho_1 \cap |\theta| \leq \frac{\beta}{2} \\ \frac{4 \sin^3 \frac{\beta}{2}}{3\pi} (\Psi_q - \rho I_{max} \gamma \sin \phi_2), & \rho_1 \leq \rho < 1 \cap |\theta| \leq \frac{\beta}{2} \\ 0, & \text{otherwise} \end{cases} \quad (10)$$

$$I_{2r} = \begin{cases} \rho I_{max} \left[ \frac{2 \sin \frac{\beta}{2} (3 - 2 \sin^2 \frac{\beta}{2})}{3\pi} + \frac{\gamma \cos \phi_2 (2\beta + \sin 2\beta)}{4\pi} \right], & 0 \leq \rho < \rho_1 \cap |\theta| \leq \frac{\beta}{2} \\ \rho I_{max} \left[ \frac{2 \sin \frac{\beta}{2} (3 - 2 \sin^2 \frac{\beta}{2})}{3\pi} + \frac{\gamma \cos \phi_2 (2 + \sin 2\beta)}{4\pi} - \frac{\Psi_r (2\beta + \sin 2\beta)}{4\pi} \right], & \rho_1 \leq \rho < 1 \cap |\theta| \leq \frac{\beta}{2} \\ 0, & \text{otherwise} \end{cases} \quad (11)$$

$$I_{2q} = \begin{cases} \rho I_{max} \gamma \sin \phi_2 \frac{2\beta - \sin 2\beta}{4\pi}, & 0 \leq \rho < \rho_1 \cap |\theta| \leq \frac{\beta}{2} \\ (-\rho I_{max} \gamma \sin \phi_2 + \Psi_q) \frac{2\beta - \sin 2\beta}{4\pi}, & \rho_1 \leq \rho < 1, |\theta| \leq \frac{\beta}{2} \\ 0, & \text{otherwise} \end{cases} \quad (12)$$

$$I_{3r} = \begin{cases} \rho I_{max} \left[ \frac{2 \sin \beta + \sin 2\beta}{4\pi} + \frac{\gamma \cos \phi_2}{5\pi} \cdot \left( 5 \sin \frac{\beta}{2} + \sin \frac{5\beta}{2} \right) \right], & 0 \leq \rho < \rho_1 \cap |\theta| \leq \frac{\beta}{2} \\ \rho I_{max} \left[ \frac{2 \sin \beta + \sin 2\beta}{4\pi} + \frac{\gamma \cos \phi_2 - \Psi_r}{5\pi} \cdot \left( 5 \sin \frac{\beta}{2} + \sin \frac{5\beta}{2} \right) \right], & \rho_1 \leq \rho < 1 \cap |\theta| \leq \frac{\beta}{2} \\ 0, & \text{otherwise} \end{cases} \quad (13)$$

$$I_{3q} = \begin{cases} -\rho I_{max} \gamma \sin \phi_2 \frac{5 \sin \frac{\beta}{2} - \sin \frac{5\beta}{2}}{5\pi}, & 0 \leq \rho < \rho_1 \cap |\theta| \leq \frac{\beta}{2} \\ -\rho I_{max} \gamma \sin \phi_2 + \Psi_q \frac{5 \sin \frac{\beta}{2} - \sin \frac{5\beta}{2}}{5\pi}, & \rho_1 \leq \rho < 1 \cap |\theta| \leq \frac{\beta}{2} \\ 0, & \text{otherwise} \end{cases} \quad (14)$$

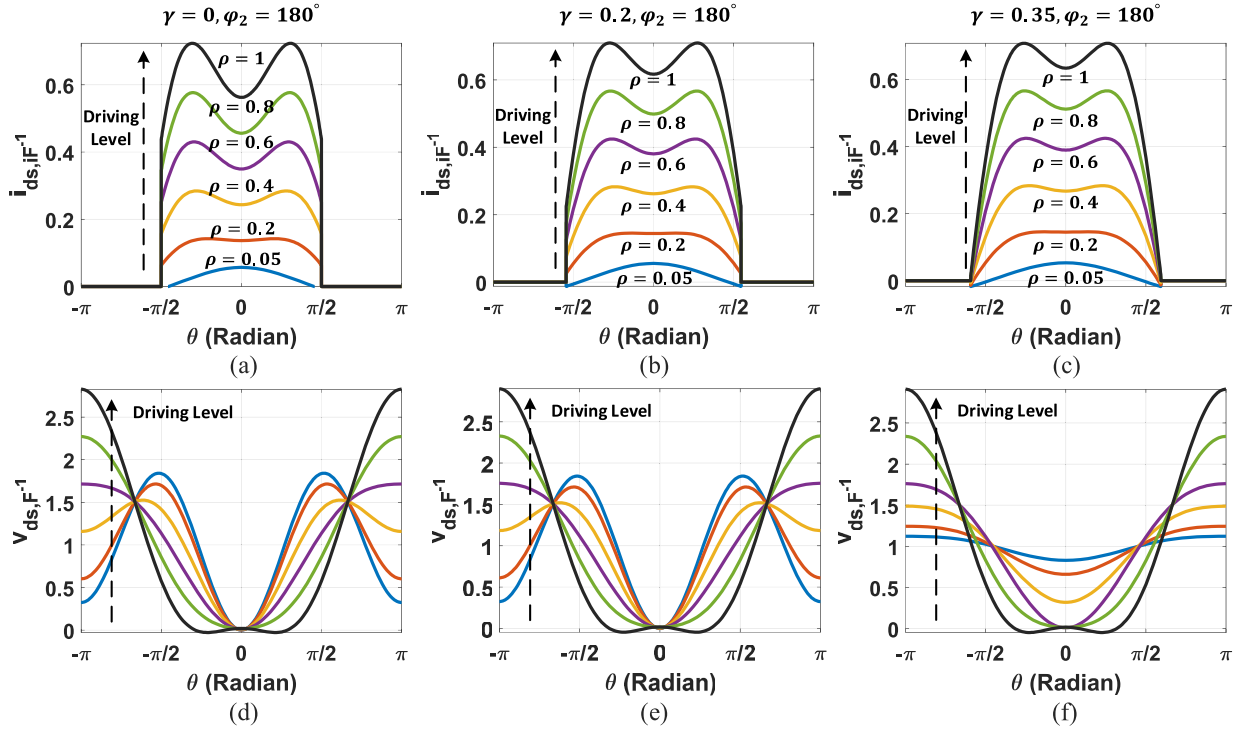


Fig. 3. Class-iF<sup>-1</sup> normalized waveforms at different driving levels for different sets of input nonlinearity parameters  $\gamma = 0, 0.2, 0.35$ , respectively, while  $\phi_2 = 180^\circ$ . (a)–(c) Drain current waveforms. (d)–(f) Drain voltage waveforms.

By substituting (9)–(12) to (18), the coefficient  $\Psi_r$  and  $\Psi_q$  of  $i_2$  can be solved and calculated as

$$\Psi_r = \frac{(V_{DD} - V_K) + \rho I_{max} \left[ \frac{\sigma_1}{6\pi} Z_{1L} + \sigma_5 Z_{2L} \right]}{\frac{\sigma_2}{3\pi} Z_{1L} + \sigma_4 Z_{2L}}$$

$$\Psi_q = \rho I_{max} \gamma \sin \phi_2 \quad (19)$$

where

$$\sigma_1 = 3\beta + 3 \sin \beta + 2\gamma \cos \phi_2 \left( 3 \sin \frac{\beta}{2} + \sin \frac{3\beta}{2} \right)$$

$$\sigma_2 = 3 \sin \frac{\beta}{2} + \sin \frac{3\beta}{2}$$

$$\sigma_3 = 2\beta + \sin 2\beta$$

$$\sigma_4 = 2 \sin \frac{\beta}{2} \left( 3 - 2 \sin^2 \frac{\beta}{2} \right)$$

$$\sigma_5 = \frac{\gamma \sigma_3 \cos \phi_2}{4\pi} + \frac{\sigma_4}{3\pi}. \quad (20)$$

As  $\phi_2$  equals to  $180^\circ$ , the value of  $\Psi_q$  becomes 0. By using (15)–(17), the generalized intrinsic drain voltage waveform can be expressed as

$$v_{DS,iF^{-1}}(\theta) = V_{DD} - [V_1 \cos \theta + V_2 \cos 2\theta + V_3 \cos 3\theta]. \quad (21)$$

Hence, the intrinsic drain voltage waveforms are plotted in Fig. 3(d)–(f). Similar to the drain current waveforms in Section II-B, when  $\gamma$  increases, the voltage waveforms become flatter, which provides a hint of how input nonlinearity changes the drain waveforms at different output power levels. Yet, it is still not enough to explain the occurrence and predict the locations of the first inflection point in the AM/AM profile.

The normalized drain current components versus output power for  $\gamma = 0, 0.2, 0.35$  are shown in Fig. 4(a)–(c), respectively. Similarly, the normalized drain voltage components are also plotted in Fig. 4(d)–(f). When the output power rises, the dc ( $I_{dc}$ ) and fundamental ( $I_{1r}$ ) drain current components increase monotonically. It is interesting to see that the position of the drain current second harmonic ( $I_{2r}$ ) first peak moves forward to a higher power level when the  $\gamma$  value increases. At the first inflection point, drain voltage hits the knee voltage and voltage swing equals  $V_{DD}$  at low input power driving level. The reason for this is the high second harmonic drain impedance causing  $V_2$  to increase at a much faster rate than  $V_1$ .

#### D. Proposed Class-iF<sup>-1</sup> PA

It is of the utmost interest to see the theoretically estimated PA performance such as the AM/AM profile and DE. Assume the source impedance is  $Z_0$ , the input power can be calculated as

$$P_{in} = \frac{1}{2} \frac{(\rho V_{GS1})^2}{Z_0} W. \quad (22)$$

The output power can be calculated as

$$P_{out} = \frac{1}{2} I_{1r}^2 \cdot Z_{1L} W. \quad (23)$$

Accordingly, the DE and power gain can be calculated as

$$\eta_{DE}(\%) = \frac{P_{out}}{I_{dc} \cdot V_{DD}} \cdot 100\%$$

$$G_{T,dB} = 10 \log \left( \frac{P_{out}}{P_{in}} \right) \text{ dB}. \quad (24)$$

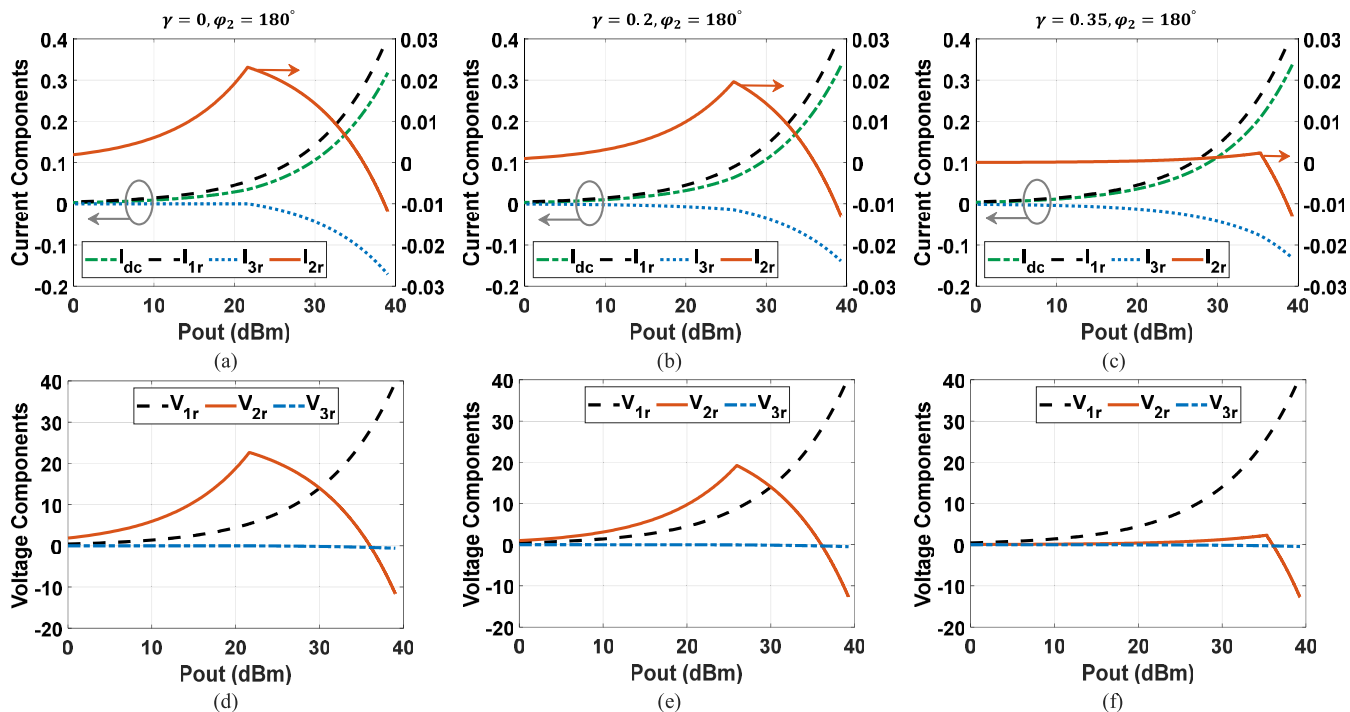


Fig. 4. (a)–(c) Normalized drain current components. (d)–(f) Drain voltage waveform components when  $\gamma = 0, 0.2, 0.35$ , respectively.

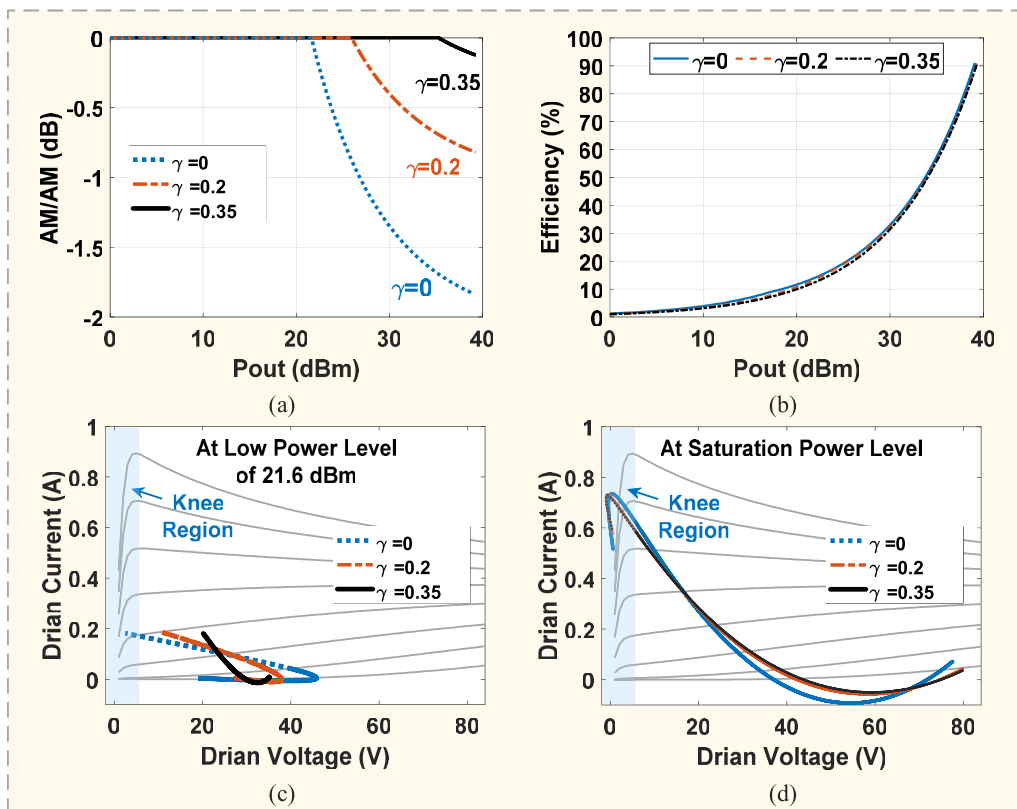


Fig. 5. Theoretical derived PA performance when  $\gamma = 0, 0.2, 0.35$ . (a) AM/AM profile and (b) efficiency versus output power; dc-IV curves and loadlines when  $\gamma = 0, 0.2, 0.35$  at (c) low power level of 21.6 dBm and (d) saturated power level.

As shown in Fig. 5(a), when  $\gamma$  increases, the AM/AM profile achieves better flatness as the first inflection point moves to the higher output power level with decreased gain compression, leading to enhanced performance in terms of

linearity, while maintaining almost the same efficiency profile, as shown in Fig. 5(b). Herein,  $\gamma = 0$  indicates the second harmonic source with short-circuit termination, referring to the conventional Class-F<sup>-1</sup>. It should be noted that a continuous

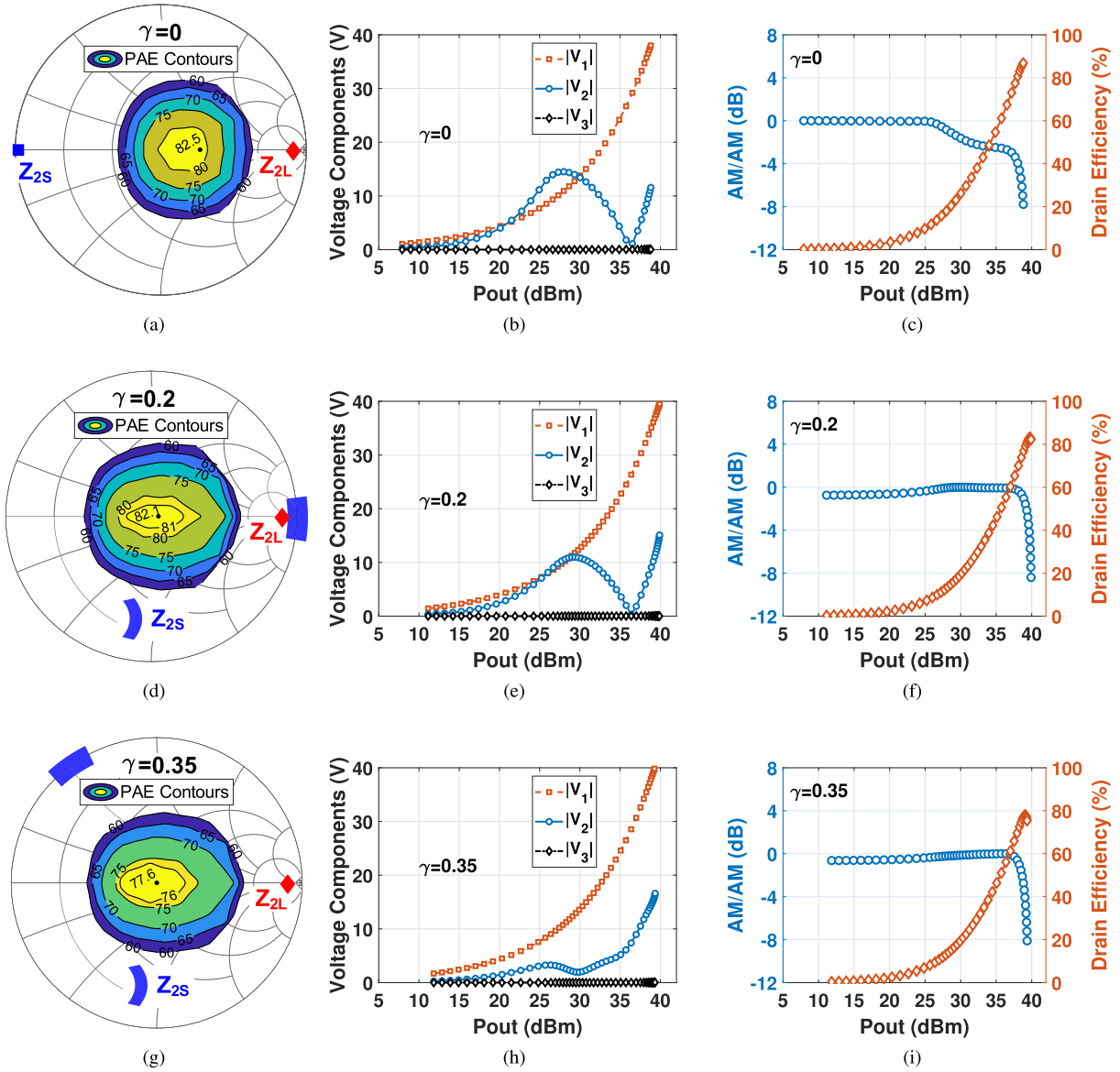


Fig. 6. Load-pull results under CW signal stimulation—PAE contour: (a)  $\gamma = 0$ , (d)  $\gamma = 0.2$ , and (g)  $\gamma = 0.35$ . Drain current components: (b)  $\gamma = 0$ , (e)  $\gamma = 0.2$ , and (h)  $\gamma = 0.35$ ; AM/AM and DE profile versus output power: (c)  $\gamma = 0$ , (f)  $\gamma = 0.2$ , and (i)  $\gamma = 0.35$ .

increase of  $\gamma$  helps push the inflection point toward a higher power region and corrects the flattens of the AM/AM profile. However, after a certain value of  $\gamma$ , over-correction will not bring further benefits. This is because the inflection point from the harmonic is pushed away to the higher power region where the compression resulting from the fundamental drain voltage and current components dominates.

As shown in Fig. 5(c), the loadline for  $\gamma = 0$  starts entering the knee region at a low power level, resulting in early gain compression, hence, the first inflection of AM/AM profile. Conversely, when the value of  $\gamma$  becomes 0.2 or 0.35, the loadline stays far from the knee region at low power and only enters the region at saturated output power level, as shown in Fig. 5(c) and (d). This phenomenon, in return, results in significant advantages of delaying the first inflection, and ultimately, eliminating the double inflection characteristic in the AM/AM profile. To practically realize the higher  $\gamma$  value, the second

harmonic source ( $Z_{2S}$ ) manipulation is required as shown in Fig. 2(b). As has been analyzed in Section II-A, when utilizing the  $\gamma$  value from 0.15 to 0.25,  $Z_{2S}$  needs to be swept over the open-circuit region with  $\angle \Gamma_{2S} = [0^\circ, 90^\circ] \cup [270^\circ, 360^\circ]$ . The  $\gamma$  value can achieve up to 0.35 when the  $\phi_2 \approx 200^\circ$ .

The AM/AM profile is then expressed by normalizing the power gain versus output power to a small-signal gain

$$\text{AM/AM} = G_{T,\text{dB}} - G_{S,\text{max,dB}} \quad (25)$$

where  $G_{S,\text{max,dB}}$  is the maximum value of the small-signal gain. By substituting (9), (15), and (22)–(24) to (25), the AM/AM profile can be predicted as a function of input drive level,  $\rho$ , and input nonlinearity parameter,  $\gamma$ .

Therefore, the PA class with the  $\gamma$  value higher than 0.15 is designated as Class-iF<sup>-1</sup> PA, which is realized by terminating  $Z_{2S}$  along the open-circuit termination at the edge of Smith chart. Hence, high saturated efficiency, low gain

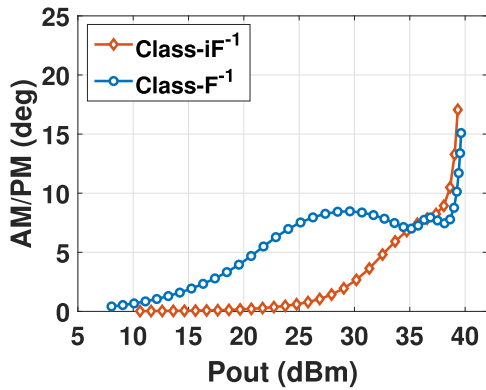


Fig. 7. AM/PM in load-pull:  $\gamma = 0$  with  $Z_{2S}$  short circuit for Class-F<sup>-1</sup>;  $\gamma = 0.2$  with  $Z_{2S}$  open circuit Class-iF<sup>-1</sup>.

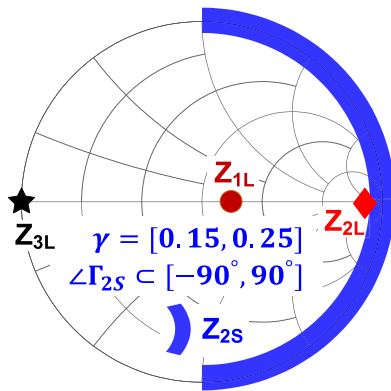


Fig. 8. Source and load design region for the proposed Class-iF<sup>-1</sup> PA operation mode.

compression level, and enhanced linearity can be achieved with the proposed Class-iF<sup>-1</sup> PA.

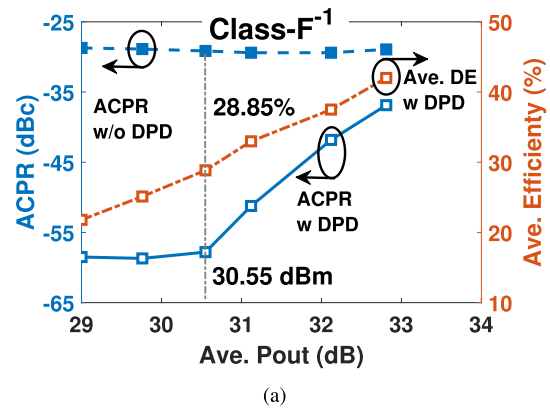
### III. LOAD—PULL ANALYSIS

To validate the performance in terms of output power, efficiency, and linearity, load-pull analyses were conducted with a 2-mm GaN device at 2.3 GHz with controlled load harmonic terminations, second harmonic load impedance ( $Z_{2L}$ ) as open, third harmonic load impedance ( $Z_{3L}$ ) as short. The fundamental load impedance ( $Z_{1L}$ ) was terminated at the maximum efficiency (MXE) point, while the fundamental source termination ( $Z_{1S}$ ) was under complex conjugate match. The drain voltage supply of the device was at 28 V and the dc quiescent current was set to 20 mA/mm.

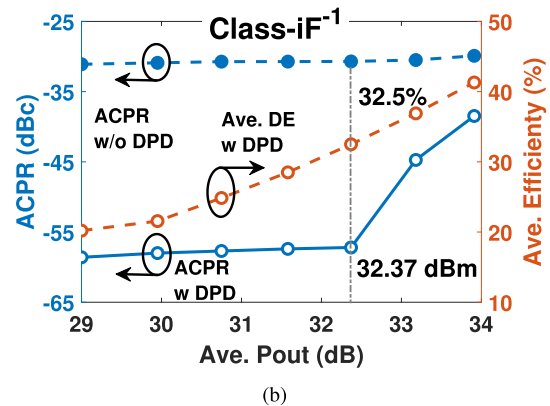
#### A. Load—Pull With CW Signal Stimulation

The load-pull was first conducted under the CW signal stimulation. The second harmonic source impedance  $Z_{2S}$  is varied by sweeping the second harmonic source phase  $\angle\Gamma_{2S}$  from 0° to 360° with  $|\Gamma_{2S}| \approx 0.9$ . Although a higher reflection coefficient is desirable,  $|\Gamma_{2S}| \approx 0.9$  is enough to extract the important source-pull data.

The parasitic parameters were de-embedded to extract the design impedance and intrinsic voltage and current waveforms at the intrinsic drain plane of the active device. The fundamental load impedance for power added efficiency (PAE) contours



(a)



(b)

Fig. 9. Load-pull with 20-MHz 8.5-dB PAPR LTE signal—ACPR and DE comparison. (a) Class-F<sup>-1</sup>. (b) Class-iF<sup>-1</sup>.

is shown in Fig. 6(a), (d), and (g). The second harmonic source terminations  $Z_{2S}$  is varied from the short-circuit point toward the open-circuit point to obtain the varied values for  $\gamma$ , while  $\phi_2$  is fixed with 180°. As a result, the second harmonic source impedance was tuned to  $Z_{2S} = 0$  ( $\angle\Gamma_{2S} = 180^\circ$ ) for  $\gamma = 0$ ,  $\angle\Gamma_{2S} = [-5^\circ, 5^\circ]$  for  $\gamma = 0.2$ , and  $\angle\Gamma_{2S} = [120^\circ, 130^\circ]$  for  $\gamma = 0.35$ .

Fig. 6(b), (e), and (h) shows the magnitude of the extracted intrinsic fundamental, second, and third harmonic drain voltage components, respectively, for the corresponding  $\gamma$  values. We can observe the variation of the second harmonic drain voltage component ( $V_2$ ) and how it is suppressed with different levels of input nonlinearity ( $\gamma$ ). For a conventional Class-F<sup>-1</sup> PA ( $\gamma = 0$ ), the drain voltage waveform swing ( $V_1 + V_2 + V_3$ ) equates to the swing value of  $V_{DD}$  and enters knee region at an early power level, as shown in Fig. 6(c). At the same time, the second harmonic component  $V_2$  hits its peak and starts to drop versus the further increased output power level. When the device loadline enters the knee region due to voltage saturation, its gain starts dropping and results in a double inflection characteristic in a conventional Class-F<sup>-1</sup> PA. When the  $\gamma$  value increases, the peak value of  $V_2$  decreases and pushes to the higher power level, which in turn results in the elimination of the first inflection point in AM/AM profile, as shown in Fig. 6(c), (f), and (i). It is interesting to see that the conventional Class-F<sup>-1</sup> achieves 37.2 dBm  $P_3$  dB (output power with 3-dB gain compression)

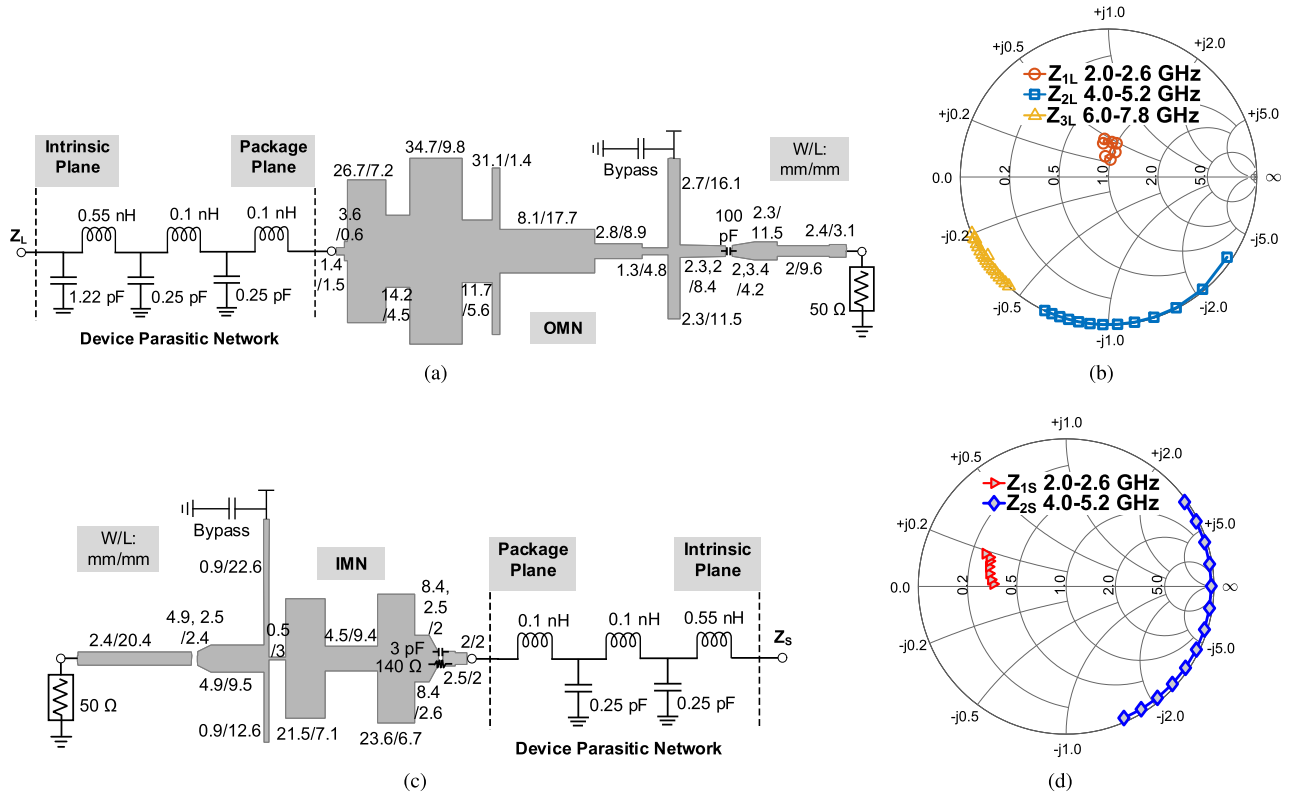


Fig. 10. (a) Schematic of output matching network. (b) Intrinsic load trajectories. (c) Schematic of input matching network. (d) Intrinsic source trajectories.

with 73.0% DE and it finally hits the peak value of 82.5% until 7.8-dB deep gain compression. The AM/AM profile is flattened for both cases when  $\gamma = 0.2$  and  $\gamma = 0.35$ , as can be seen from Fig. 6(f) and (i). Moreover, the amplitude-to-phase modulation (AM/PM) profile for the proposed Class-iF<sup>-1</sup> PA is compared to the conventional Class-F<sup>-1</sup> PA, as is shown in Fig. 7. The proposed Class-iF<sup>-1</sup> PA shows a monotonous AM/PM profile which is highly desirable.

Compared to Class-F<sup>-1</sup>, the proposed Class-iF<sup>-1</sup> ( $\gamma \geq 0.15$ ) has much less compression at the same saturation power level, showing enhanced linearity performance. These load—pull validations provide a comprehensive insight into the mathematical derivation versus power driving level in Section II.

In consistency to [29], a broad design space with source second harmonic around the open-circuit region is confirmed, where excellent gain flatness can be achieved. Based on the comprehensive analysis and load—pull simulation, a generalized second harmonic source design space is concluded and shown in Fig. 8 for the proposed Class-iF<sup>-1</sup>, which is along the open-circuit region ( $\angle \Gamma_{2S}$  inside  $[-90^\circ, 90^\circ]$ ) on the smith chart.

### B. Load—Pull With Modulated Signal Stimulation

To further evaluate the performance in terms of output power, efficiency, and linearity in the practical wireless communication system, load—pull simulation was also conducted under the stimulation of modulated signal. The comparison was performed between the conventional Class-F<sup>-1</sup> ( $\gamma = 0$ ) and Class-iF<sup>-1</sup> ( $\gamma = 0.2$ ). A 20-MHz long-term-evolution (LTE) signal with 8.5-dB peak-to-average power

TABLE I

PERFORMANCE COMPARISON BETWEEN CLASS-F<sup>-1</sup> AND CLASS-iF<sup>-1</sup> PAs UNDER MODULATED SIGNAL STIMULATION

Parameters	Class-F <sup>-1</sup> PA	Class-iF <sup>-1</sup> PA
Max. Linearizable Ave. Pout (dBm)	30.55	32.37
Max. Linearizable Ave. DE (%)	28.85	32.5
ACPR w/o DPD (dBc)	-29.2	-30.7
ACPR w DPD (dBc)	-57.8	-57.2

Max. linearizable: ACPR lower than -55 dBc with DPD.

ratio (PAPR) was used for the test. The memory polynomial-based (MP) digital predistortion (DPD) was performed with the same complexity to evaluate the linearizability of both PAs. Fig. 9(a) and (b) shows that the adjacent channel power ratios (ACPRs) were  $\sim -29.1$  dBc for Class-F<sup>-1</sup> and  $\sim -30.7$  dBc for Class-iF<sup>-1</sup> when the average output power (ave. Pout) varies from 29.0 to 33.0 dBm. After applying DPD, the Class-iF<sup>-1</sup> PA can achieve up to 32.37 dBm average output power and 32.5% average efficiency with -57.2 dBc ACPR. As concluded in Table I, compared with the Class-F<sup>-1</sup> PA, the Class-iF<sup>-1</sup> PA has improved average output power ( $\sim +1.8$  dBm) and average efficiency ( $\sim +3.6\%$ ) while maintaining the ACPR lower than -55 dBc after DPD correction. Therefore, the utilization of open-circuit second harmonic source termination significantly improved the performance in terms of average output power, average efficiency, and linearity under the modulated signal stimulation for the proposed Class-iF<sup>-1</sup> PA.

## IV. PROTOTYPE AND EXPERIMENTAL RESULTS

As a proof of concept, an RF-input Class-iF<sup>-1</sup> PA was designed and fabricated from 2.0 to 2.6 GHz, using a GaN

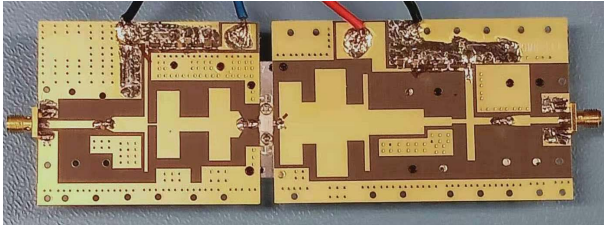


Fig. 11. Photograph of the fabricated Class- $iF^{-1}$  PA.

HEMT (CG2H40010F) from Wolfspeed. The designed PA was realized on a 31-mil-thick Taconic TLY-5 substrate with a 2.2 dielectric constant.

Fig. 10(a) and (c) shows the output matching network and input matching network. To extract the intrinsic source/load impedance, the de-embedded network for the CG2H40010F transistor was utilized. The intrinsic trajectories shown in Fig. 10(b) indicate the typical Class- $F^{-1}$  load conditions. As shown in Fig. 10(d), it can be seen that the intrinsic second harmonic source impedance  $Z_{2S}$  is over the open-circuit region, which follows the theoretical design space of the proposed Class- $iF^{-1}$ .

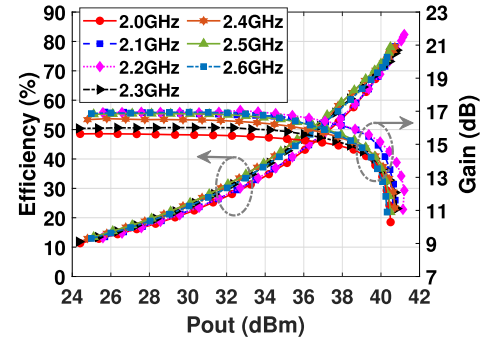
Fig. 11 presents the photograph of the fabricated PA. The drain supply voltage of 28 V and total quiescent current of 5 mA were set during all the measurements. The CW and modulated signals were both generated by a vector signal generator, and the output power was measured with a spectrum analyzer. A broadband linear driver amplifier was used to drive the PA with enough input power. A broadband circulator was added between the driver and the PA to improve isolation.

### A. Measurement Results With CW Signal

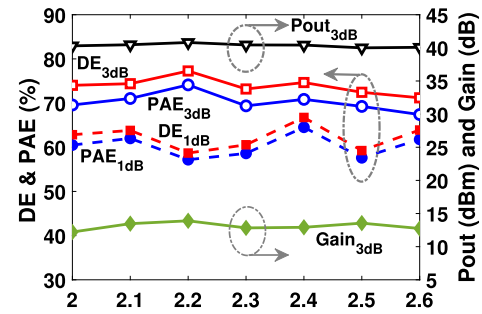
The PA was first measured under CW signal stimulation. Fig. 12(a) presents the measured DE and gain versus output power at different operating frequencies. The measured DE, PAE, output power, and gain at 3-dB gain compression ( $P_{3\text{dB}}$ ) level versus operation frequencies are presented in Fig. 12(b). From 2.0 to 2.6 GHz, the proposed Class- $iF^{-1}$  PA can achieve 40.1–40.8-dBm output power, 71.2%–77.3% DE, and 67.4%–74.1% PAE at  $P_{3\text{dB}}$  level. Moreover, Fig. 12(b) also shows 58.7%–66.7% DE and 57.2%–64.5% PAE at 1-dB gain compression ( $P_{1\text{dB}}$ ). Therefore, high saturation efficiency and flat gain response over the operation bandwidth are obtained.

### B. Measurement Results With Modulated Signals

To evaluate the linearity and efficiency performance under modulated signal stimulation, 20- and 100-MHz LTE signals with 8.5-dB PAPR were used to test the PA. Fig. 13(a) presents the output spectrum with and without DPD linearization at 2.3 GHz with the 20-MHz signal. The measured ACPRs were  $-28.03/-27.61$  dBc without DPD. After applying DPD, the ACPRs were improved to  $-56.05/-56.10$  dBc, with around 32.01 dBm average output power and 34.59% average DE. The AM/AM and AM/PM characteristics with and without DPD are given in Fig. 13(b). Under the stimulation of the 100-MHz signal, the measured ACPRs were  $-22.99/-21.66$  dBc without DPD and  $-48.76/-48.21$  dBc with DPD correction at



(a)



(b)

Fig. 12. Measured results under the CW signal test. (a) DE and gain versus output power. (b) DE, PAE, output power, and gain versus frequency at 3- and 1-dB gain compression levels.

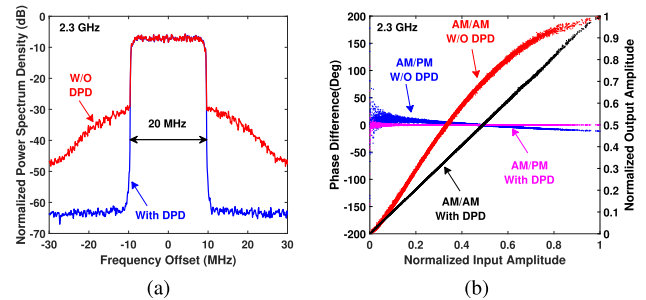


Fig. 13. Performance with and without DPD correction of the proposed Class- $iF^{-1}$  PA at 2.3 GHz with 20-MHz 8.5-dB PAPR LTE signal. (a) Output spectrum. (b) AM/AM and AM/PM.

2.3 GHz as shown in Fig. 14(a). Around 31.80 dBm average output power and 34.21% average DE were obtained after applying DPD. The AM/AM and AM/PM characteristics with and without DPD are also given here in Fig. 14(b).

### C. Performance Comparison

Table II summarizes the performance of some recently reported PAs with high saturated efficiency. Compared with other published work, the proposed Class- $iF^{-1}$  PA shows good DE and PAE, which are extracted at  $P_{3\text{dB}}$  level. Furthermore, from 2.0 GHz to 2.6 GHz, the PA has only  $\pm 0.35$  dBm variation in terms of  $P_{3\text{dB}}$ . The modulated signal test results are compared with previously published Class- $F^{-1}/F$  papers in

TABLE II  
PERFORMANCE COMPARISON WITH RECENT STATE-OF-THE-ART HIGH EFFICIENCY PAS

Ref. (Year)	Tech. /	Freq. (GHz)	$P_{out}$ (dBm)	DE (%)	PAE (%)	Class of PA	Signal BW (MHz)	PAPR (dB)	$P_{ave}$ (dBm)	DE @ave (%)	ACPR wo DPD (dBc)	ACPR w DPD (dBc)
[14] 2012	GaN	1.45-2.45	40.4-42.3	70-81	N/A	Class-F	40	6.5*	35.7	46.2	-24.9	-49.4
[34] 2013	GaN	0.53-1.33	39.0-41.4	70-87	N/A	Class-F	15	11.6	29.8	N/A	-35.2	-48.5
[35] 2015	GaN	1.7-2.8	40.2-42.9	60.3-80.3	N/A	Class-F <sup>-1</sup>	100	9.0*	32.1	30.5	-34.0	-46.0
[36] 2016	GaN	1.35-2.5	41.1-42.5	68-82	N/A	Class-F <sup>-1</sup>	20	7.0	34.6	37	-26.4	-45.2
[37] 2017	GaN	0.5-0.95	38-40	73-79	70-76	Class-F <sup>-1</sup>	5	N/A	33	32	-35	N/A
[23] 2019	GaN	0.8-1.4	38-42.3	75-93	73-82	Class-F <sup>-1</sup>	20	11.25	N/A	N/A	-27.3	-52.2
[38] 2020	GaN	3.4-3.6 3.5-3.75	38.5-40.0 ≤ 38.5	N/A N/A	63-67 60-66	Class-F <sup>-1</sup>	3.84	6.5	N/A	N/A	N/A	N/A
This work	GaN	2.0-2.6	40.1-40.8	71.2-77.3	67.4-74.1	Class-iF <sup>-1</sup>	20	8.5	32.01	34.59	-27.61	-56.05
							100	8.5	31.80	34.21	-21.66	-48.21

\*Back-off power

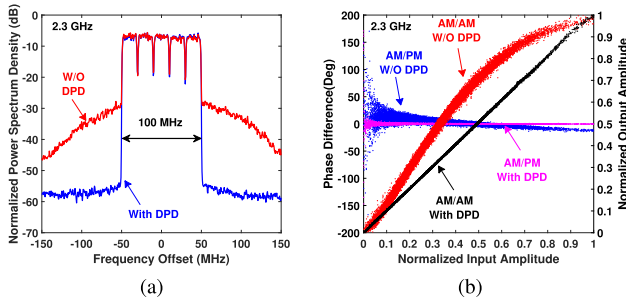


Fig. 14. Performance with and without DPD correction of the proposed Class-iF<sup>-1</sup> PA at 2.3 GHz with 100-MHz 8.5-dB PAPR LTE signal. (a) Output spectrum. (b) AM/AM and AM/PM.

Table II as well. Under the stimulation of 100-MHz modulated signal, the proposed Class-iF<sup>-1</sup> PA showed  $-48.21$  dBc ACPR after DPD correction and achieved about 4% higher average DE compared with the previously reported Class-F<sup>-1</sup> PA in [35].

## V. CONCLUSION

In this article, we presented a new class of PA, designated as Class-iF<sup>-1</sup>, with enhanced linearity compared to the conventional Class-F<sup>-1</sup> PA. For the first time, the drain current/voltage waveforms and AM/AM profile are modeled as a function of power driving level and input nonlinearity. Theoretical derivation and load–pull results show that different levels of input nonlinearity result in the alternation of the AM/AM inflection points, which can be ultimately controlled with second harmonic source ( $Z_{2S}$ ) manipulation. A Class-iF<sup>-1</sup> PA was designed and fabricated using packaged GaN device. Measured 40.1–40.8-dBm output power, 71.2%–77.3% DE, and 67.4%–74.1% PAE were achieved at 3-dB gain compression level over 2.0–2.6 GHz.

## REFERENCES

- [1] F. H. Raab, "Class-F power amplifiers with maximally flat waveforms," *IEEE Trans. Microw. Theory Techn.*, vol. MTT-45, no. 11, pp. 2007–2012, Nov. 1997.
- [2] P. Colantonio, F. Giannini, G. Leuzzi, and E. Limiti, "High efficiency low-voltage power amplifier design by second-harmonic manipulation," *Int. J. RF Microw. Comput.-Aided Eng.*, vol. 10, no. 1, pp. 19–32, Jan. 2000.
- [3] P. J. Tasker, "Practical waveform engineering," *IEEE Microw. Mag.*, vol. 10, no. 7, pp. 65–76, Dec. 2009.
- [4] P. Colantonio, F. Giannini, and E. Limiti, *High Efficiency RF and Microwave Solid State Power Amplifiers*. New York, NY, USA: Wiley, 2009.
- [5] J. H. Kim, G. D. Jo, J. H. Oh, Y. H. Kim, K. C. Lee, and J. H. Jung, "Modeling and design methodology of high-efficiency class-F and class-F<sup>-1</sup> power amplifiers," *IEEE Trans. Microw. Theory Techn.*, vol. 59, no. 1, pp. 153–165, Jan. 2011.
- [6] J. Moon, S. Jee, J. Kim, J. Kim, and B. Kim, "Behaviors of class-F and class-F<sup>-1</sup> amplifiers," *IEEE Trans. Microw. Theory Techn.*, vol. 60, no. 6, pp. 1937–1951, Jun. 2012.
- [7] J. C. Pedro, L. C. Nunes, and P. M. Cabral, "A simple method to estimate the output power and efficiency load–pull contours of class-B power amplifiers," *IEEE Trans. Microw. Theory Techn.*, vol. 63, no. 4, pp. 1239–1249, Apr. 2015.
- [8] A. Grebennikov and F. H. Raab, "History of class-F and inverse class-F techniques: Developments in high-efficiency power amplification from the 1910s to the 1980s," *IEEE Microw. Mag.*, vol. 19, no. 7, pp. 99–115, Nov. 2018.
- [9] S. C. Cripps, P. J. Tasker, A. L. Clarke, J. Lees, and J. Benedikt, "On the continuity of high efficiency modes in linear RF power amplifiers," *IEEE Microw. Wireless Compon. Lett.*, vol. 19, no. 10, pp. 665–667, Oct. 2009.
- [10] P. Wright, J. Lees, J. Benedikt, P. J. Tasker, and S. C. Cripps, "A methodology for realizing high efficiency class-J in a linear and broadband PA," *IEEE Trans. Microw. Theory Techn.*, vol. 57, no. 12, pp. 3196–3204, Dec. 2009.
- [11] V. Carrubba et al., "On the extension of the continuous class-F mode power amplifier," *IEEE Trans. Microw. Theory Techn.*, vol. 59, no. 5, pp. 1294–1303, May 2011.
- [12] N. Tuffy, A. Zhu, and T. J. Brazil, "Class-J RF power amplifier with wideband harmonic suppression," in *IEEE MTT-S Int. Microw. Symp. Dig.*, Jun. 2011, pp. 1–4.
- [13] V. Carrubba et al., "The continuous inverse class-f mode with resistive second-harmonic impedance," *IEEE Trans. Microw. Theory Techn.*, vol. 60, no. 6, pp. 1928–1936, Jun. 2012.

- [14] N. Tuffy, L. Guan, A. Zhu, and T. J. Brazil, "A simplified broadband design methodology for linearized high-efficiency continuous class-F power amplifiers," *IEEE Trans. Microw. Theory Techn.*, vol. 60, no. 6, pp. 1952–1963, Jun. 2012.
- [15] K. Chen and D. Peroulis, "Design of broadband highly efficient harmonic-tuned power amplifier using in-band continuous class-F<sup>-1</sup>/F mode transferring," *IEEE Trans. Microw. Theory Techn.*, vol. 60, no. 12, pp. 4107–4116, Dec. 2012.
- [16] T. Cannin, P. J. Tasker, and S. Cripps, "Continuous mode power amplifier design using harmonic clipping contours: Theory and practice," *IEEE Trans. Microw. Theory Techn.*, vol. 62, no. 1, pp. 100–110, Jan. 2014.
- [17] M. Yang, J. Xia, Y. Guo, and A. Zhu, "Highly efficient broadband continuous inverse class-F power amplifier design using modified elliptic low-pass filtering matching network," *IEEE Trans. Microw. Theory Techn.*, vol. 64, no. 5, pp. 1515–1525, May 2016.
- [18] T. Sharma et al., "High-efficiency input and output harmonically engineered power amplifiers," *IEEE Trans. Microw. Theory Techn.*, vol. 66, no. 2, pp. 1002–1014, Feb. 2018.
- [19] S. K. Dhar, T. Sharma, R. Darraji, M. Helaoui, and F. M. Ghannouchi, "On the continuity of continuous inverse class F power amplifiers," in *IEEE MTT-S Int. Microw. Symp. Dig.*, Dec. 2018, pp. 1–3.
- [20] T. Sharma et al., "On the efficiency and AM/AM flatness of inverse class-F power amplifiers," in *IEEE MTT-S Int. Microw. Symp. Dig.*, Jun. 2019, pp. 460–463.
- [21] S. K. Dhar, T. Sharma, N. Zhu, D. Holmes, R. Darraji, and F. M. Ghannouchi, "Comprehensive analysis of input waveform shaping for efficiency enhancement in class B power amplifiers," in *IEEE MTT-S Int. Microw. Symp. Dig.*, Jun. 2019, pp. 1164–1167.
- [22] T. Sharma et al., "Simplified first-pass design of high-efficiency class-F<sup>-1</sup> power amplifiers based on second-harmonic minima," *IEEE Trans. Microw. Theory Techn.*, vol. 67, no. 7, pp. 3147–3161, Jul. 2019.
- [23] S. K. Dhar et al., "Investigation of input–output waveform engineered continuous inverse class F power amplifiers," *IEEE Trans. Microw. Theory Techn.*, vol. 67, no. 9, pp. 3547–3561, Sep. 2019.
- [24] S. K. Dhar et al., "Input-harmonic-controlled broadband continuous class-F power amplifiers for sub-6-GHz 5G applications," *IEEE Trans. Microw. Theory Techn.*, vol. 68, no. 7, pp. 3120–3133, Jul. 2020.
- [25] S. K. Dhar et al., "Impact of input nonlinearity on efficiency, power, and linearity performance of GaN RF power amplifiers," in *IEEE MTT-S Int. Microw. Symp. Dig.*, Aug. 2020, pp. 281–284.
- [26] S. K. Dhar et al., "Modeling of input nonlinearity and waveform engineered high-efficiency class-F power amplifiers," *IEEE Trans. Microw. Theory Techn.*, vol. 68, no. 10, pp. 4216–4228, Oct. 2020.
- [27] T. Sharma, S. Shukla, D. G. Holmes, R. Darraji, J. K. Jones, and F. Ghannouchi, "Input harmonic sensitivity in high-efficiency GaN power amplifiers," in *IEEE MTT-S Int. Microw. Symp. Dig.*, Jun. 2018, pp. 461–464.
- [28] T. Sharma, J. Roberts, D. G. Holmes, R. Darraji, J. K. Jones, and F. M. Ghannouchi, "On the double-inflection characteristic of the continuous-wave AM/AM in class-F<sup>-1</sup> power amplifiers," *IEEE Microw. Wireless Compon. Lett.*, vol. 28, no. 12, pp. 1131–1133, Dec. 2018.
- [29] C. Chu, S. K. Dhar, T. Sharma, and A. Zhu, "Class-iF<sup>-1</sup>: Linearity enhanced high efficiency power amplifier," in *Proc. IEEE Topical Conf. RF/Microw. Power Modeling Microw. Radio Wireless Appl. (PAWR)*, Jan. 2022, pp. 39–41.
- [30] P. M. White, "Effect of input harmonic terminations on high efficiency class-B and class-F operation of PHEMT devices," in *IEEE MTT-S Int. Microw. Symp. Dig.*, vol. 3, Jun. 1998, pp. 1611–1614.
- [31] J. J. Bussgang, L. Ehrman, and J. W. Graham, "Analysis of nonlinear systems with multiple inputs," *Proc. IEEE*, vol. 62, no. 8, pp. 1088–1119, Aug. 1974.
- [32] P. Colantonio, F. Giannini, G. Leuzzi, and E. Limiti, "Multiharmonic manipulation for highly efficient microwave power amplifiers," *Int. J. RF Microw. Comput.-Aided Eng.*, vol. 11, no. 6, pp. 366–384, Nov. 2001.
- [33] B. M. Merrick, J. B. King, and T. J. Brazil, "The continuous harmonic-tuned power amplifier," *IEEE Microw. Wireless Compon. Lett.*, vol. 25, no. 11, pp. 736–738, Nov. 2015.
- [34] Lu, Zisheng, and W. Chen, "Resistive second-harmonic impedance continuous class-F power amplifier with over one octave bandwidth for cognitive radios," *IEEE J. Emerg. Sel. Topics Circuits Syst.*, vol. 3, no. 4, pp. 489–497, Apr. 2013.
- [35] Y. Sun and X. Zhu, "Broadband continuous class-F<sup>-1</sup> amplifier with modified harmonic-controlled network for advanced long term evolution application," *IEEE Microw. Wireless Compon. Lett.*, vol. 25, no. 4, pp. 250–252, Apr. 2015.

- [36] M. Yang, J. Xia, Y. Guo, and A. Zhu, "Highly efficient broadband continuous inverse class-F power amplifier design using modified elliptic low-pass filtering matching network," *IEEE Trans. Microw. Theory Techn.*, vol. 64, no. 5, pp. 1515–1525, May 2016.
- [37] Y. Dong, L. Mao, and S. Xie, "Extended continuous inverse class-F power amplifiers with class-AB bias conditions," *IEEE Microw. Wireless Compon. Lett.*, vol. 27, no. 4, pp. 368–370, Apr. 2017.
- [38] L.-H. Zhou, X. Y. Zhou, W. S. Chan, T. Sharma, and D. Ho, "Wideband class-F<sup>-1</sup> power amplifier with dual-/quad-mode bandpass response," *IEEE Trans. Circuits Syst. I, Reg. Papers*, vol. 67, no. 7, pp. 2239–2249, Jul. 2020.



**Chenhao Chu** (Member, IEEE) received the M.S. degree (Hons.) in electronic information engineering from the City University of Hong Kong (CityU), Hong Kong, China, in 2017. He is currently pursuing the Ph.D. degree in electronic engineering at University College Dublin (UCD), Dublin, Ireland.

From October 2017 to September 2018, he was a Research Assistant with the State Key Laboratory of Millimeter Waves, Department of Electronic Engineering, CityU. He is currently with the RF and Microwave Research Group, School of Electrical and Electronic Engineering, UCD. His research interests include broadband high-efficiency power amplifiers, MMIC power amplifier design for RF/mm-wave applications, and antenna-in-package (AiP) for phased arrays.

Mr. Chu has won three prizes in IEEE Microwave Theory and Technology Society (MTT-S) High Efficiency Power Amplifier Student Design Competitions (HEPA-SDCs), that is, the Second Place at the 2021 International Microwave Symposium (IMS2021), the First Place for both ACPR-FoM and EVM FoM at 2022 Radio and Wireless Week (RWW2022), and the Third Place at IMS2022. He was also on the final list of the Student Paper Competition at RWW2022 and Three-Minute Thesis Competition (3MT) at IMS2022. He was also a recipient of the Best Student Paper Award (First Place) of the 19th Royal Irish Academy/the International Union of Radio Science (RIA/URSI) Research Colloquium on Radio Science and Communications in October 2022. He is a Reviewer of journals, including IEEE TRANSACTIONS ON MICROWAVE THEORY AND TECHNIQUES, IEEE TRANSACTIONS ON CIRCUITS AND SYSTEMS—I: REGULAR PAPERS, and *IEEE Microwave Magazine*.



**Vivek Tamrakar** (Member, IEEE) received the B.E. degree in electrical and electronics engineering from Chhattisgarh Swami Vivekanand Technical University, Bhilai, Chhattisgarh, India, in 2012, and the M.Tech. degree in electrical engineering from the Maulana Azad National Institute of Technology, Bhopal, India, in 2015. He is currently pursuing the Ph.D. degree with a specialization in communication and signal processing (RF and microwave) at the Department of Electrical Engineering, IIT Bombay, Mumbai, India.

From July 2016 to December 2017, he was an Assistant Professor with the SSGI Faculty of Engineering and Technology, Bhilai. His research interests include broadband high-efficiency power amplifiers, continuous mode harmonic controlled power amplifiers at S-band, and waveform engineering.



**Sagar K. Dhar** (Member, IEEE) received the Ph.D. degree in electrical and computer engineering from the iRadio Laboratory, University of Calgary, Calgary, AB, Canada, in 2020.

He is currently working as a Staff RF Design Engineer with Renesas Electronics, San Diego, CA, USA, developing power amplifiers (PAs) for 5G infrastructures. He has also worked as a Senior RF Application Design Engineer with Macom Technologies Canada Inc., Toronto, Canada, developing high-efficiency/linear PAs for high-power base station requirements. His current research interests include high-efficiency RF power amplifiers, Doherty power amplifiers, large signal device modeling, digital signal processing, and load-pull techniques.

Dr. Dhar was a recipient of the Izaak Walton Killam Pre-Doctoral Scholarship, the AITF Doctoral Scholarship, the Open Doctoral Scholarship, the Transformative Talent Internship Award, the Academic Excellence Award, and the Research Productivity Award.



**Tushar Sharma** (Member, IEEE) received the Ph.D. degree in electrical engineering from the University of Calgary, Calgary, AB, Canada, in 2018.

Following his Ph.D. degree, he was a Post-Doctoral Researcher with the Integrated Micro-Systems Research Laboratory, Princeton University, Princeton, NJ, USA. He is currently a Staff RF Engineer with Renesas Electronics, San Diego, CA, USA, and a Visiting Professor with IIT Bombay, Mumbai, India. He has more than 45 publications in international journals and conferences along with four granted patents. His research interests include high-frequency novel reconfigurable techniques in RF and mm-wave transmitters, broadband high-power gallium nitride (GaN) power amplifiers, large signal device modeling, technology characterization, digital signal processing, mm-wave amplifiers, and waveform engineering.

Dr. Sharma was a recipient of the IMS 2020 Best Industry Paper Award, the 2019/2020 IMS Best Student Paper Award, the Izaak Walton Killam Pre-Doctoral Scholarship, the Alberta Science and Innovation under 30 Future Leader Award, the Alberta Innovates Technology Future Doctoral Scholarship, the Alberta Transformative Talent Scholarship, the IEEE Education Activity Board Pre-Educator Award, the IEEE MGA Young Professionals Achievement Award, and the University of Calgary 2018 Early Achievement Alumni Award.



**Jayanta Mukherjee** (Senior Member, IEEE) received the B.Eng. degree from the Birla Institute of Technology, Mesra, India, in 1999, and the M.S. and Ph.D. degrees in electrical and computer engineering from The Ohio State University, Columbus, OH, USA, in 2003 and 2006, respectively.

He is currently a Professor with the Department of Electrical Engineering, IIT Bombay, Mumbai, India. His research interests include RFIC design, testing, and modeling.

Dr. Mukherjee was a Texas Instruments Fellow from 2001 to 2005. He has received the University Gold Medal at the Birla Institute of Technology for the highest GPA in his major.



**Anding Zhu** (Fellow, IEEE) received the Ph.D. degree in electronic engineering from the University College Dublin (UCD), Dublin, Ireland, in 2004.

He is currently a Professor with the School of Electrical and Electronic Engineering, UCD. His research interests include high-frequency nonlinear system modeling and device characterization techniques, high-efficiency power amplifier design, wireless transmitter architectures, digital signal processing, and nonlinear system identification algorithms.

Prof. Zhu is an Elected Member of the IEEE Microwave Theory and Technology Society (MTT-S) Administrative Committee (AdCom) and a member of the IEEE Future Directions Committee. He was a recipient of the 2021 IEEE MTT-S Microwave Prize. He has served as the Secretary for the IEEE MTT-S AdCom in 2018 and the Chair for IEEE MTT-S Microwave High-Power Techniques Committee (TC-12) in 2020 and 2021. He is a Track Editor of IEEE TRANSACTIONS ON MICROWAVE THEORY AND TECHNIQUES and an Associate Editor of *IEEE Microwave Magazine*.